Engineered $BaTiO_3/SnIn_4S_8$ step–scheme nanocomposite with interfacial coupling for energy-efficient piezo-photocatalytic oxidation of tetracycline

Tshepo T. Mohlala[1], *Tunde* L. Yusuf[2], *Mike* Masukume[3], *Vincent* Ojijo[3], and *Nonhlangabezo* Mabuba[1,4*1]

[1]University of Johannesburg, Department of Chemical Science, Doornfontein Campus, Johannesburg, 2028, South Africa
[2]Department of Chemistry, Faculty of Natural and Agricultural Sciences, University of Pretoria, Private Bag X20, Hatfield 0028, Pretoria, South Africa
[3]Council for Scientific and Industrial Research (CSIR), Pretoria Campus, Pretoria, 0001, South Africa
[4]Centre for Nanomaterial Science Research, Department of Chemical Sciences, Doornfontein Campus, Johannesburg, 2028, South Africa

Abstract. Tetracycline hydrochloride (TCH) has been recognized as one of the most problematic pollutants in water systems due to its extensive uses in medical and veterinary systems. Poor removal leads to persistent residues that lead to antibiotic resistance and ecological disruption. The nanosphere-on-nanoflower architecture of $BaTiO_3/SnIn_4S_8$ (BTO/SIS) was designed and fabricated via solvothermal synthesis using ethanol as a solvent, as an energy-efficient catalyst for piezo-phototronic applications. Characterization such as Mott-Schottky (M-S), scanning electron microscopy (SEM), and XRD were used to substantiate the nanoflower-decorated nanosphere composite heterojunction contact leading to the Step-scheme (S-scheme) band alignment promoting partial recombination through the internal electric field for enhanced charge separation, generation, and migration within the heterostructure. Owing to the synergistic effects of the S-scheme alignment and the hierarchical morphology, BTO/SIS (1:1) ratio achieved the removal of ~85% of the persistent tetracycline hydrochloride (TCH) in 120 minutes with minimal 70 W light illumination and low ultrasonication power of 6.8 W (20 kHz). The optimized BTO/SIS possessed a synergistic factor of 1.74 (>1), way higher than the single photocatalytic and piezocatalytic processes. Photoluminescence (PL), and electrochemical impedance spectroscopy (EIS) indicated longer lifetimes of charge carriers, lower charge transfer resistance, and lower rates of recombination. Interestingly, TCH as an amphoteric molecule was efficiently removed at an optimum pH of 7 where it is at its zwitterionic form. Trapping studies revealed that superoxides ($\bullet O_2^-$) were the major oxidants responsible for the degradation caused by efficient electron transfer and via indirect oxidation especially in S-scheme heterojunctions. This study not only demonstrated the energy-efficient 0D/3D BTO/SIS system but also showed that the nanosphere piezoelectric BTO with a photo-active nanoflower in an architecture S-scheme enhances mechanical deformation sensitivity, while maintaining high stability in piezo-photocatalytic degradation of organic pollutants in water.
Keywords: Tetracycline (TCH); $SnIn_4S_8$; Piezoelectric; Piezo-photocatalytic; $BaTiO_3$; S-Scheme

1 Introduction

The persistent escalation of antibiotic consumption, driven by increasing human and animal populations, poses profound environmental challenges [1]. These antibiotic molecules exhibit remarkable chemical stability due to their robust molecular frameworks, rendering them highly resistant to natural degradation in aquatic environments. Such environmental persistence significantly contributes to the emergence of antibiotic resistance, disrupting the delicate balance of aquatic ecosystems and threatening biodiversity [1].

Moreover, beyond ecological perturbations, antibiotics like tetracycline adversely impact agricultural productivity by inhibiting plant growth and provoke unintended physiological responses in exposed organisms [2]. TC is ubiquitously detected in various water bodies including lakes, rivers, and ponds largely

*Nonhlangabezo Mabuba: nmabuba@uj.ac.za

due to substantial anthropogenic inputs from pharmaceutical manufacturing effluents, domestic wastewater discharge, aquaculture operations, and agricultural runoff [3]. Its intrinsic chemical stability under ambient environmental conditions curtails biodegradation and complicates removal processes in conventional wastewater treatment. Tetracycline also strongly adsorbs onto sediment and soil matrices, extending environmental residence times from days to several months. Ecotoxicological investigations demonstrated Tetracycline's toxicity toward aquatic organisms such as algae, daphnia, and fish by impeding enzymatic functions and photosynthetic processes, thereby destabilizing essential ecosystem services [4]. Chronic pharmaceutical contamination frequently induces microbial community imbalance and oxidative stress, heightening risks of deoxyribose nucleic acid (DNA) damage under sustained exposure.

Conventional remediation approaches like photodegradation are limited by sluggish reaction rates and high energy consumption due to reliance on UV irradiation [5]. Additionally, tetracycline forms complexes with metal ions, which modulate its solubility and bioavailability, further constraining treatment efficiency. In this context, semiconductor-based advanced oxidation technologies have emerged as promising, sustainable ("green") alternatives for environmental detoxification [5]. These materials have been extensively explored for photocatalytic and piezocatalytic degradation of organic pollutants in aqueous media. Despite their potential, challenges persist, including inadequate photostability, piezoelectric stability, low electrical conductivity, and suboptimal charge carrier separation and transfer [6]. Heterojunction engineering represents a powerful strategy to mitigate these limitations by enhancing visible-light absorption, piezo-potential generation, conductivity, and improving interfacial charge dynamics.

Among piezocatalysts, barium titanate ($BaTiO_3$) is notable for its high catalytic efficiency and superior charge carrier diffusion characteristics [7]. However, its wide electronic band gap impairs effective charge separation, resulting in elevated electron-hole recombination rates. Coupling $BaTiO_3$ with narrow band gap semiconductors has demonstrated significant improvements in photo- and piezo-photocatalytic performance under visible light and ultrasonic irradiation, expanding applicability in environmental remediation [6].

Tin indium sulfide ($SnIn_4S_8$, SIS), a ternary transition metal sulfide semiconductor, has emerged as an attractive catalyst for diverse applications owing to its unique electronic properties [8]. Nevertheless, SIS suffers from intrinsically low surface area and rapid electron-hole recombination, limiting catalytic efficiency, with its piezocatalytic potential remaining underexplored. Rational material design and engineering offer routes to optimize SIS as a bifunctional catalyst capable of driving both oxidative and reductive reactions.

In this study, we present a facile solvothermal synthesis protocol to fabricate pure SIS, $BaTiO_3$ (BTO), and their heterojunction composites in varying proportions for effective tetracycline degradation. An S-scheme heterojunction architecture was engineered by embedding $BaTiO_3$ nanorods within $SnIn_4S_8$ nanosheets, promoting synergistic piezo-photocatalytic activity against tetracycline Comprehensive electrochemical, piezo-electrochemical, and structural characterizations elucidated enhanced interfacial charge transfer and improved catalytic performance.

The $BaTiO_3/SnIn_4S_8$ composites showcase integrated nanoflower and nanosphere morphologies synthesized via ethanol-mediated solvothermal methods. Optimal composite ratios identified by transient piezo-photocurrent measurements were systematically employed for multi-antibiotic oxidation, demonstrating robust catalytic versatility and environmental applicability.

2 Materials and methods

2.1 Materials

All chemicals were of analytical grade and used without further purification. Sodium sulfate (Na_2SO_4, Extrapure AR, s, 99.5%) was obtained from Sisco Research Laboratories Pvt. Ltd., along with tetracycline hydrochloride (TC, s, $C_{22}H_{24}N_2O_8 \cdot HCl$), titanium ethoxide (ET, aq, $C_8H_{20}O_4Ti$, 30–35%), thioacetamide (CH_3CSNH_2, s, 98%), and sodium hydroxide (NaOH, s, 99.5%). Barium chloride dihydrate ($BaCl_2 \cdot 2H_2O$, s, 99.0%), polyvinylidene fluoride (PVDF, aq, 99.0%), N-methyl-2-pyrrolidone (NMP, s, 99.0%), potassium chloride (KCl, s, 99%), polyvinylpyrrolidone (PVP, s, average molecular weight 360,000), potassium hexacyanoferrate(II) tetrahydrate ($K_4Fe(CN)_6 \cdot 3H_2O$, s, 98.5%), acrylamide solution (C_3H_5NO, 40% aq, electrophoresis grade), potassium hexacyanoferrate(III) ($K_3Fe(CN)_6$, s, >99.0% ACS reagent), indium chloride ($InCl_2$, s, 98%), ethylene glycol (EG, aq, 99.8%), tert-butanol (t-BuOH, 99.7%, aq, ACS reagent), formic acid (HCOOH, aq, 98%), tin(II) chloride (s, 98%), and disodium ethylenediaminetetraacetic acid (EDTA-2Na, s, 98%) were purchased from Sigma Aldrich (USA).

2.2 Synthesis of Barium Titanate ($BaTiO_3$, BTO)

The barium titanate (BTO) hybrid nanospheres were prepared by hydrothermal synthesis, whereby 4.40 g of $BaCl_2 \bullet 2H_2O$ was weighed and dissolved in deionized water [9]. Titanium ethoxide (ET, 0.55 ml) was dissolved in 10 ml of ethylene glycol. The two solutions were mixed at room temperature, followed by the addition of 10 ml NaOH (10 M), and the solution was allowed to stir for 30 minutes. Deionized water was added to reach the final volume of 60 ml of solution and transferred into a Teflon-lined autoclave and heated at 200 degrees Celsius for 24 hours. The solution was allowed to cool at room temperature the centrifuged to collect the white

precipitate, then washed with ethanol and deionized water several times, respectively. BTO powder was dried at 60 °C overnight.

2.3 Synthesis of Barium titanate tin indium sulfide ($BaTiO_3/SnIn_4S_8$, BTO/SIS)

Synthesis of composite nanostructures of BTO/SIS was accomplished via the solvothermal process. 2 mmol of BTO was weighed and dissolved in 25 mL of ethanol and stirred for a few minutes [10]. Then, 2 mmol of $SnCl_2•2H_2O$ and $InCl_4•4H_2O$ were weighed and added to the mixture with continuous stirring until completely dissolved. Thioacetamide (2 mmol) was then added and stirred for 30 minutes before being transferred into a Teflon-lined autoclave and heated in a muffle furnace for 12 hours at 160 °C. After cooling the mixtures to room temperature, the precipitates were collected via centrifugation and washed several times with absolute ethanol and deionized water. Different ratios were also synthesized, namely, BTO/SIS (1:1), BTO/SIS (5:4), and BTO/SIS (5:2) along with SIS without the addition of BTO.

2.4 Characterization

X-ray diffraction (XRD) analysis was performed using an Advanced diffractometer equipped with Cu Kα radiation (λ = 154.18 pm, Rigaku Ultima IV, Japan) to investigate the structural properties of the materials. The surface features of the samples were examined through scanning electron microscopy (SEM, VEGA 3 TESCAN, Czech Republic), while transmission electron microscopy (TEM, JEM-2100, JEOL, Japan) was employed to study the internal morphology and crystallinity of the nanostructures. Optical characteristics of the catalysts were assessed using UV–visible diffuse reflectance spectroscopy (UV-Vis DRS, Cary60, Agilent, USA). The Brunauer–Emmett–Teller (BET) method (Micromeritics TriStar II, Germany) was applied to measure the specific surface area, pore volume, and pore size distribution. Photoluminescence (PL) spectra were recorded with a SHIMADZU RF-6000 spectro-fluorophotometer (Japan) to evaluate charge transfer and recombination behavior. Electrochemical studies, including transient photocurrent response, linear sweep voltammetry (LSV), electrochemical impedance spectroscopy (EIS), and Mott–Schottky (M-S) analysis, were carried out using an Autolab electrochemical workstation with NOVA 2.1 software (Netherlands) under visible light irradiation (70 W solar simulator, Republic of South Africa). A 0.3 M Ag/AgCl electrode served as the reference, platinum wire was used as the counter electrode, and the working electrode was prepared by drop-casting the catalyst slurry onto fluorine-doped tin oxide (FTO) substrates. The slurry was obtained by mixing 50 mg of catalyst powder with 5 wt.% PVDF and 100 µL/mL NMP, applied to the conductive side of FTO (1.5 cm × 1.5 cm), and dried overnight at 60 °C. For LSV and photocurrent measurements, 0.1 M Na_2SO_4 was used as the electrolyte (bias potential = 1.5 V), while EIS and M-S analyses employed 5 mM $[Fe(CN)_6]^{3-}$ in 0.1 M KCl solution. Piezocurrent measurements were conducted in a three-electrode configuration with 0.1 M Na_2SO_4 as the electrolyte. Ultrasonication was performed using a 500 W VCX500 ultrasonicator at 6.8 W output, 20% amplitude, for 200 s with 10 s ON–OFF cycles. For piezo-photocurrent studies, the light source remained on while ultrasonication was intermittently applied.

2.5 Photocatalytic evaluation

The piezo-photocatalytic activity of the catalyst was examined by monitoring the degradation of TCH under simultaneous ultrasonication and light irradiation. A VCX500 ultrasonicator (500 W) was employed to deliver mechanical energy, with an ice bath used to stabilize the reaction temperature, while a 70 W visible lamp provided illumination. In a typical experiment, 30 mg of catalyst was dispersed in 80 mL of TCH solution (5 mg L^{-1}) and stirred in the dark for 30 minutes to establish adsorption-desorption equilibrium. The reaction was then initiated by applying ultrasonication at 6.8 W (20 kHz) together with solar lamp illumination for 120 minutes, during which 3 mL aliquots were withdrawn every 30 minutes. Concentration changes and absorbance were measured using a Cary 60 UV–Vis spectrophotometer. The degradation efficiency was calculated using the equation(1):

$$(\%)\ \text{Degradation efficiency} = \frac{C_0 - C_t}{C_0}\ x\ 100 \quad (1)$$

where C_0 is the initial concentration at time zero and C_t is the concentration at a given interval. Further analysis of degradation products after piezo-photocatalytic treatment with BTO/SIS (1:1) was performed using ultra-performance liquid chromatography coupled with a SYNAPT G1 mass spectrometer (Waters, USA).

3 Discussion and Results

3.1 Optical properties and charge transfer

Optical properties of as-prepared nanostructures (BTO, SIS, BTO/SIS (1:1), BTO/SIS (5:4), and BTO/SIS (5:2)) were investigated using Ultraviolet-visible diffuse reflectance spectra (UV-vis-DRS) and photoluminescence spectra (PL), electrochemical properties through charge carrier dynamics using electrochemical impedance spectroscopy (EIS), Mott-Schottky (M-S), and transient photocurrent response (TRP), electrochemical analysis to determine photo-properties, charge separation, charge migration, and interfacial relation between the 0D BTO and 3D SIS (**Fig. 1**). The absorption edge of SIS was located at ≈590 nm in the visible spectra, indicating a significant visible light

absorption compared to BTO which is near the UV-region (≈390 nm) (**Fig. 1(a)**). Introduction of 3D nanoflowers into 0D nanospheres showed improved light absorption exhibited by the highest photo-absorption by BTO/SIS (1:1) behind pristine SIS, indicating enhanced light-harvesting properties. Sulfide loading highlights the interfacial relationship between the BTO and SIS through shielding and light trapping properties as shown red and blue shifts. Furthermore, energy band gaps of the nanostructures were determined using the Tauc plot as shown in **Fig. 1(b)**. The determination of the band gap applies the assumption that the energy-dependent absorption α can be expressed by equation (2) [11]:

$$(\alpha h\nu)^{1/n} = B(h\nu - E_g) \quad (2)$$

Where *h* is Planck's constant (6.626×10^{-34}/4.35×10^{-15} eVs), *v* is the photon's frequency (s^{-1}), B is a constant, and E_g is the band gap (eV). The type of electronic transition is indicated with n = ½ for indirect transitions and n = 2 for direct transitions. From the absorption spectra obtained using the P. Kubelka and F. Munk theory, band gaps were extrapolated from the x-axis on the steep linear increase of the plots. Cubic BTO shows an indirect band gap, while SIS has a direct band gap. Indirect Tauc plots give band gaps of 2.98 for BTO and 1.79 eV for SIS, the latter being smaller as expected for metal sulfides and favoring visible-light harvesting. Incorporating SIS into BTO systematically narrows the band gap across all composites, with BTO/SIS (1:1) showing the most favorable optical response. Photoluminescence (excitation ≈390 nm) reveals that pristine BTO has the highest PL intensity, indicating strong e^-/h^+ recombination. Adding SIS lowers PL intensity, evidencing enhanced charge separation, with BTO/SIS (1:1) giving the most efficient separation under visible light (**Fig. 1(c)**).

TPR measurements show BTO/SIS (1:1) has the highest photocurrent density (0.053 mA/cm²), confirming improved light absorption and catalytic activity, further boosted slightly by combined light and ultrasound (**Fig. 1(e)**). EIS Nyquist plots show SIS has the lowest R_{ct} (highest conductivity), while BTO has a large R_{ct} due to its dielectric nature. Composites 5:4 and 5:2 show larger semicircles linked to interfacial polarization. BTO/SIS (1:1) balances conductive (SIS) and dielectric (BTO) contributions, indicating optimized charge mobility and electrochemical behavior (**Fig. 1(f)**).

The confirmation of the semiconductor type was evaluated using the Mott-Schottky (M-S) plot for both the pristine BTO, and SIS (**online Fig.**). The experimental M-S plots indicate that BTO and SIS are both n-type due to the increasing/positive slopes [12]. Extrapolated flat band potential of BTO and SIS were -0.46 and -1.33 V vs Ag/AgCl, respectively. For n-type semiconductors, it has been reported that the conduction band is 0.1-0.3 eV above the flat band (E_{FB}) potential [13]. The conversion of Ag/AgCl to NHE was accomplished using equations (3):

$$E_{FB\ (vs.\ NHE)} = E_{FB\ (vs.\ Ag/AgCl)} + E_{Ag/AgCl} + 0.059pH \quad (3)$$

$$E_{VB} = E_{CB} + E_g \quad (4)$$

Where E_{CB}, E_{VB}, and E_g are the conduction band, valence band, and band gap, respectively. Converted flat band potentials of BTO and SIS were estimated to be 0.12 and -0.75 V vs NHE, respectively. It is reported that the conduction band is estimated to be 0.1-0.3 V from the Fermi energy level. When the estimation is applied, the conduction band is positioned at 0.021 and -0.85 V vs. NHE for BTO and SIS, respectively. Valence band edges were calculated using equation 4 using the indirect band gap transitions from the Tauc plot, where the valence band was 3.00 for BTO and 0.94 V for SIS. By utilization of the band edges calculations, the band positions of the pristine nanostructures in the composite arrangement can be illustrated (**online Fig.**).

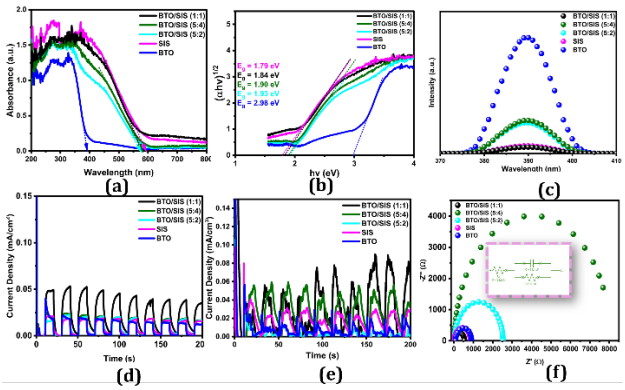

Fig. 1. (a) UV-vis DRS, (b) Tauc plot, (c) PL, (d) photocurrent, (e) piezo-photocurrent, and (f) EIS of BTO, SIS, BTO/SIS (1:1), BTO/SIS (5:4), and BTO/SIS (5:2).

The optimal composite ratio was identified using electrochemical and piezo-electrochemical analyses, which showed that BTO/SIS (1:1) has superior optical, piezoelectric, and piezo-phototronic properties compared with pristine materials and other composites (BTO/SIS (5:4), BTO/SIS (5:2)). Consequently, BTO/SIS (1:1) was selected for further study. Detailed characterization by FE-SEM, TEM, and BET confirmed its structural integrity, surface chemistry, and electronic structure, providing a solid basis for reliably evaluating its piezo-photocatalytic degradation performance.

3.2 X-ray diffraction (XRD) and morphological analysis

X-ray diffraction measurements were used for the phase purities and structural properties of the synthesized BTO, SIS, and BTO/SIS composites (**Fig. 2(a-b)**). In the pristine SIS nanostructures, the diffraction peaks are indexed as (220), (311), (222), (400), (440), and (531) for $SnIn_4S_8$ cubic, (JCPD: 00-042-1306), respectively. For the pristine $BaTiO_3$, the diffraction peaks at 22°, 23°, 25°, 28°, 32°, 34°, 38°, 41°, 43°, 46°, 47°, 56°, and 65° correspond to (100), (110), (111), (200), (211), (220), and (300) planes of cubic $BaTiO_3$, respectively (JCPD: 04-028-0370). The BTO/SIS (1:1) heterostructure indicated

the presence of both the SIS and BTO, as indicated in **Fig. 2(a),** and the integration of peaks in the composite crystallography. The presence of all the characteristic peaks of each semiconductor substantiates the successful synthesis of the heterojunction.

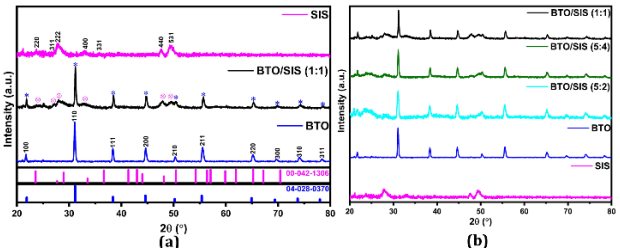

Fig. 2. XRD of (a) BTO, SIS, and BTO/SIS (1:1), (b) SIS, BTO, and BTO/SIS composites.

The fabricated nanostructures were examined using FE-SEM and TEM to characterize the external and internal morphology of the as-prepared nanostructures. FE-SEM images (**Fig. 3(a**) show the nanoflowers of SIS (200 nm) consisting of a random assortment of nanoflakes. FE-SEM micrograph of BTO (**Fig. 3(b)**), however, shows spherical nanostructures and concentrated clusters indicating signs of agglomeration; when SIS was introduced to form a heterostructure, the nanoflowers self-assembled with the spherical nanostructures of BTO on the surfaces of the SIS thin sheets, making up the flaps of the flower-like structure (**Fig. 3(c)**). The pore structure of SIS was maintained in the BTO/SIS (1:1) heterostructure with the potential some of nanospheres being embedded inside the nanoflower pores.

The 1D nanosheets making the nanoflowers were observed on the TEM micrographs (**Fig. 3(d)**) highlight their smooth surface. BTO exhibited nanospheres as observed in SEM possessing smooth contours (**Fig. 3(e)**). The BTO nanospheres also indicated aggregated clusters with some interparticle voids shown by the presence of some darker, some lighter particles, and more finely textured areas which are associated with nanocrystals. Interestingly, the composite (BTO/SIS) showed the nanoflower folds along a long backbone (**Fig. 3(f)**). The wrinkled sheets of the SIS had some nanospheres (BTO) on the surface with some spread around the sheets revealing a hierarchical structure (**Fig. 3(f)**: x100 insert).

Energy dispersive spectroscopy (EDS) was used for the determination of the elements Ba, Ti, and O belonging to the $BaTiO_3$ and Sn, In, and S belonging to $SnIn_4S_8$, both were present in the binary composite signifying successful fabrication of a heterostructure. The corresponding percentages, O (24.6 wt%), In (23.8 wt%), Ti (15.0 wt%), Sn (14.4 wt%), S (13.6 wt%), and Ba (8.5 wt%) are consistent with the composite heterostructure formation (**online Fig.**).

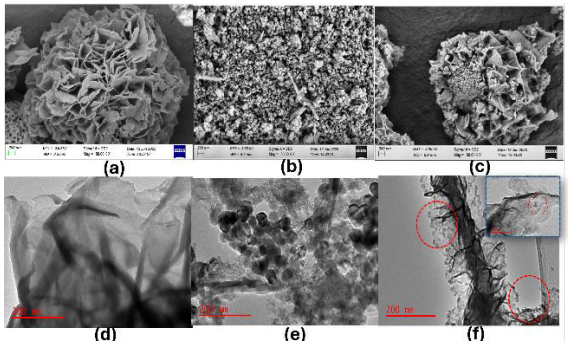

Fig. 3. FE-SEM micrographs of (a) SIS, (b) BTO, and (c) BTO/SIS (1:1), and TEM of (d) SIS, (e) BTO, and (f) BTO/SIS (1:1).

3.3 Braunauer-Emmett-Teller Analysis

Nitrogen adsorption–desorption (BET/BJH) was used to evaluate the porosity of BTO, SIS, and BTO/SIS composites (**Fig. 4**). All samples show type IV isotherms with H3 hysteresis loops, confirming mesoporosity (2–50 nm). Pristine BTO and SIS have surface areas of 3.87 and 11.82 m^2/g, respectively **(Fig. 4(a))**. Incorporating SIS into BTO markedly increases the BET surface area, peaking at 184.73 m^2/g for BTO/SIS (5:4), then slightly decreasing at 1:1, giving a volcano-type trend that is mirrored by the pore volume **(Fig. 4(b))**. Smaller pore diameters are associated with higher surface area and pore volume, indicating that the 5:4 and 1:1 composites possess finer, more uniform mesoporous networks, whereas the 5:2 ratio has fewer, larger pores, consistent with its lower surface area.

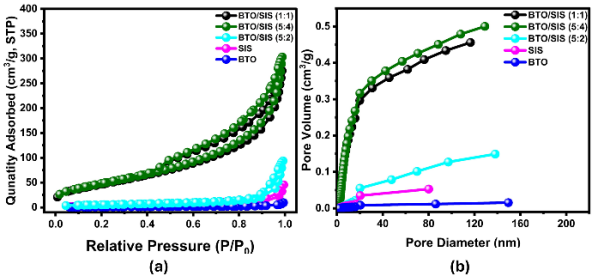

Fig. 4. (a) Nitrogen adsorption-desorption isotherms and (b) pore size vs pore volume of BTO, SIS, BTO/SIS (1:1), BTO/SIS (5:4), and BTO/SIS (5:2).

Table 1. BET surface area and BJH pore volume and diameter

Samples	Surface Area (m^2/g)	Pore Diameter (nm)	Pore Volume (cm^3/g)
BTO	3.8694	15.402	0.014899
SIS	11.821	23.796	0.070322
BTO/SIS (1:1)	178.58	9.53667	0.42576
BTO/SIS (5:4)	184.73	10.1507	0.46878
BTO/SIS (5:2)	19.667	29.489	0.14499

3.4 Piezo-Photocatalytic performance

Piezo-photocatalytic degradation of TCH was carried out under visible light (70 W) and ultrasound (6.8 W) using 30 mg of catalyst for 150 min, following a 30 min dark adsorption-desorption equilibrium. Aliquots (3 mL) were withdrawn every 15 min and analyzed by UV-vis spectroscopy at ~356 nm to monitor concentration decay (**Fig. 5(a)**). Dark adsorption showed that BTO/SIS (5:4) achieved the highest removal (54.72%) due to its large surface area, followed by pristine SIS (49.02%), while bare BTO and the 5:2 and 1:1 composites adsorbed less than 30% of TCH (**online Fig**). Under light, BTO/SIS (5:4) again performed best (60% removal), with SIS (42%) and BTO/SIS (1:1) (39.6%) indicating an additional ~6% removal from photocatalytic oxidation beyond adsorption (**Fig. 5(b)**). Similar trends appeared under ultrasound (**Fig. 5(c)**), and in the combined system (stirring + light + ultrasound) BTO/SIS (1:1) showed the highest overall degradation (~85%), confirming its superior piezo-photocatalytic synergy, while BTO/SIS (5:4) remained optimal mainly for adsorption (**Fig. 5(d)**). The reaction kinetics were assessed using a pseudo-first-order kinetic model using equation (2):

$$\ln\left({}^{C_0}/_{C_t}\right) = kt \quad (2)$$

where C_0, C_t, t, and k represent original concentration, concentration at time t, time in minutes, and rate of degradation, respectively. The rate constants (k) were determined from the slopes of the kinetic plots $\ln(C_t/C_0)$ vs time (t) as shown (**online Fig.**). Obtained from the plots, the rate constants were 0.00119, 0.00307, 0.0263, and 0.01614 min^{-1}, for adsorption, piezocatalysis, photocatalysis, and piezo-photocatalysis, respectively. Higher k values demonstrate faster, higher, and efficient removals when the hybrid process (piezo-photocatalysis) is employed. The synergistic effects between photocatalysis and piezocatalysis were quantified using the synergistic factor and synergy percentage, using the following equation (3):

$$\mathrm{SF} = \frac{k_{app}\ (\text{Piezocatalysis} - \text{Photocatalysis})}{k_{app}\ (\text{piezocatalysis}) + k_{app}\ (\text{Photocatalysis})} \quad (3)$$

Where the k_{app} is the degradation rate of each application. The synergistic factor was calculated to be 2.83. The SF value for the hybrid process exceeds 1 (2.83), proving positive synergy between the photocatalytic and piezocatalytic effects.

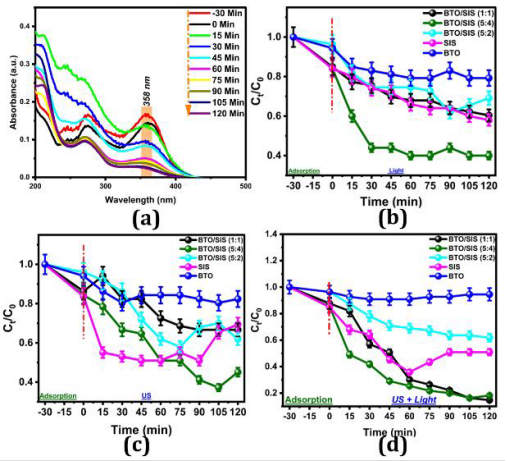

Fig. 5. (a) UV-vis absorption of TCH, (b) photocatalysis, (c) piezocatalysis, and (d) piezo-photocatalysis using BTO/SIS (1:1), BTO/SIS (5:4), BTO/SIS (5:2), SIS, and BTO.

3.5 Trapping studies and effect of pH

Piezo-photocatalytic degradation mechanism was determined through evaluation of the main active degradation species: Hydroxyl radicals (•OH), holes (h^+), and superoxide radicals ($•O_2^-$). Ethylenediaminetetraacetic acid disodium salt (EDTA-2Na), acrylamide, and tert-butyl alcohol (t-BuOH) were used as trapping agents for h^+, $•O_2^-$, and •OH, respectively. Piezo-photocatalytic degradation of tetracycline hydrochloride (TCH) proceeds predominantly via superoxide radicals ($•O_2^-$), as evidenced by the pronounced inhibition of degradation upon acrylamide addition (**Fig. 6(a)**). Hole scavenging (EDTA-2Na) induces a moderate activity loss, whereas hydroxyl radical quenching (t-BuOH) has only a minor effect, indicating a reactivity order of $•O_2^- > h^+ >$ •OH for the overall process.

Solution pH strongly modulates degradation by altering both TCH speciation and catalyst surface charge. Near-neutral pH (7), where TCH is zwitterionic, affords the highest degradation efficiency due to an optimal balance between adsorption and oxidative attack (**Fig. 6(b)**). In alkaline conditions (pH 10), efficiency drops sharply despite similar adsorption, while at pH 3 enhanced adsorption of cationic TCH coincides with reduced degradation, likely due to less favorable conditions for •OH-based oxidation. Consequently, all kinetic evaluations were conducted at pH 7 to represent the intrinsic catalytic performance.

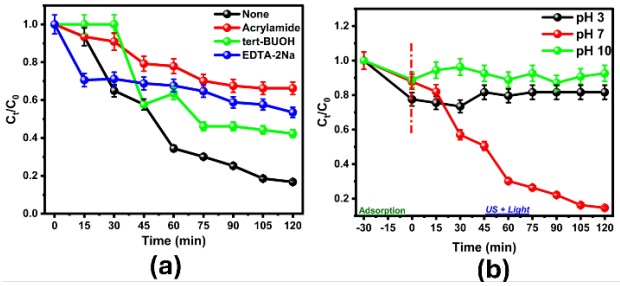

Fig. 6. (a) Trapping studies and (b) pH studies

3.6 Proposed mechanism of degradation of TCH

The piezo-photocatalytic degradation pathway of TCH over BTO/SIS (1:1) in water is outlined in **Fig. S4**. The band gaps (Eg) of pristine BTO and SIS, obtained from UV-vis DRS and Tauc plots using the Kubelka–Munk method, are 2.98 and 1.79 eV, respectively. Band-edge positions (E_{VB}, E_{CB}) were derived from Mott-Schottky (M–S) analysis using the flat-band potential (E_{FB}) to estimate the Fermi level (E_F) and band edges. E_{FB} values measured vs Ag/AgCl were converted to the NHE scale, giving 0.12 V (BTO) and −0.75 V (SIS). For these n-type semiconductors, the E_{CB} values were calculated as -0.85 V (SIS) and 0.0021 V (BTO), and E_{VB} values as 0.94 (SIS) and 3.0 V (BTO). These results show that SIS has a much more negative E_{CB} than BTO, identifying SIS as the reductive catalyst (RC) and BTO as the oxidative catalyst (OC). Therefore, electrons flow from SIS to BTO under illumination and piezoelectric polarization, driving TCH degradation through spatially separated redox sites and not light and ultrasound (**online Fig.**).

$$\text{BTO/SIS (1:1)} + hv + US \rightarrow e^- + h^+ \quad (4)$$

$$\text{SIS } (e^-) + O_2 \rightarrow {}^{\bullet}O_2^- \quad (5)$$

$$\text{BTO } (h^+) + OH^- \rightarrow {}^{\bullet}OH \quad (6)$$

$$US + H_2O \rightarrow {}^{\bullet}OH + H^+ \quad (7)$$

$$\text{BTO } (h^+) + H_2O \rightarrow {}^{\bullet}OH + H^+ \quad (8)$$

$${}^{\bullet}O_2^- + h^+ + {}^{\bullet}OH + \text{TCH} \rightarrow H_2O + CO_2 + \text{Small molecules} \quad (9)$$

4 Conclusion

In this work, we reported the synthesis and hierarchical formation of the piezoelectric effect and Step-Scheme nanostructures through the solvothermal fabrication route. The random arrangement of the 3D nanoflowers of SIS conferred a temporary piezoelectric effect on the metal sulfide, as indicated by the high transient piezocurrent density response and Nyquist plots obtained under ultrasonication and illumination. The nano-spherical 0D BTO exhibited good photo-properties due to its nanoparticle nature, which is beneficial for photocatalytic applications. The composite with the most optimal conditions was BTO/SIS (1:1), which showed higher light absorption via UV-DRS, a higher piezo-current density, and a smaller charge transfer resistance. Combined effects of light illumination, ultrasonication, and step-scheme band alignment indicated a synergistic effect in piezo-photocatalysis, resulting in sufficient generation of oxidants capable of breaking TCH using BTO/SIS (1:1). The catalyst's efficiency was further corroborated by the low power utilisation and high sensitivity, moderate catalyst and high removal of TCH. In this work, new perspectives on the heterojunction formation between the integration of piezo-phototronic properties and the Step-Scheme development between metal oxides and sulfides are highlighted for the treatment of persistent organic pollutants via the piezo-photocatalytic degradation process.

Mohlala Tshepo T.: Writing – review & editing, Writing – original draft, Formal analysis, Data curation, Conceptualisation. Tunde L. Yusuf: Writing – review & editing, Writing – original draft, Supervision, Conceptualisation. Masukume Mike: Writing – original draft, Project administration. Ojijo Vincent: Writing – original draft, Project administration. Mabuba Nonhlangabezo: Writing – review & editing, Writing – original draft, Resources, Project administration, Conceptualisation.

The authors declare that there are no conflicts of interest

We thank the Centre for Nanomaterials Science Research, University of Johannesburg (UJ), South Africa, and the Faculty of Science. TTM is grateful to the Council for Scientific and Industrial Research (CSIR), South Africa, for the study grant, CPRR Grant Number.

References

1. K. Samal, S. Mahapatra, and M. Hibzur Ali, Pharmaceutical wastewater as Emerging Contaminants (EC): Treatment technologies, impact on environment and human health, Energy Nexus **6**, 100076 (2022).
2. W. Han, Y. Liu, X. Liang, J. Liu, Q. Jiang, C. Zhang, and Y. Zhang, A Trojan Horse in the soil: Tetracycline hijacks plant organellar ribosomes to stunt growth and unbalance the rhizosphere microecology, J. Hazard. Mater. **510**, 141792 (2026).
3. T. H. Grossman, Tetracycline Antibiotics and Resistance, Cold Spring Harb. Perspect. Med. **6**, a025387 (2016).
4. D. E. Brodersen, W. M. Clemons, A. P. Carter, R. J. Morgan-Warren, B. T. Wimberly, and V. Ramakrishnan, The Structural Basis for the Action of the Antibiotics Tetracycline, Pactamycin, and Hygromycin B on the 30S Ribosomal Subunit, Cell **103**, 1143 (2000).
5. T. Bekele and G. Alamnie, The photocatalytic degradation of organic pollutants a comprehensive overview, Results Chem. **18**, 102758 (2025).
6. J.-Y. Yin and C. Sun, Harnessing piezo-potential in photocatalysis: Fundamental mechanisms, material fabrication, and environmental engineering solutions, J. Environ. Chem. Eng. **13**, 119042 (2025).
7. X. Liu, L. Xiao, Y. Zhang, and H. Sun, Significantly enhanced piezo-photocatalytic capability in $BaTiO_3$ nanowires for degrading organic dye, J. Materiomics **6**, 256–262 (2020).
8. Y. Zhang, X. Liu, X. Zhang, L. Liu, T. Li, H. Yang, and W. Li, Indium sulfide-sensitized 2D stannum indium sulfide nanosheet arrays promoting photoelectrochemical conversion efficiency in cathodic protection, Mater. Today Energy **42**, 101563 (2024).

9. M. Inada, N. Enomoto, K. Hayashi, J. Hojo, and S. Komarneni, Facile synthesis of nanorods of tetragonal barium titanate using ethylene glycol, Ceram. Int. **41**, 5581 (2015).
10. M. Lu, Z. Sun, Y. Zhang, Q. Liang, M. Zhou, S. Xu, and Z. Li, Construction of cobalt phthalocyanine sensitized $SnIn_4S_8$/g-C_3N_4 composites with enhanced photocatalytic degradation and hydrogen production performance, Synth. Met. **268**, 116480 (2020).
11. D. Chawla and N. Goswami, Structural and optical properties of CdZnS nanoparticles by exploding wire technique, Mater. Today Proc. **28**, 278 (2020).
12. C. Zhao, C. Shao, X. Li, X. Li, R. Tao, X. Zhou, and Y. Liu, Magnetically separable Bi_2MoO_6/$ZnFe_2O_4$ heterostructure nanofibers: Controllable synthesis and enhanced visible light photocatalytic activity, J. Alloys Compd. **747**, 916 (2018).
13. T. T. Mohlala, T. L. Yusuf, M. Masukume, V. Ojijo, and N. Mabuba, Enhanced piezo-induced photocatalytic activity of $BaTiO_3$/$Cd_{0.5}Zn_{0.5}S$ Sscheme heterojunction for water pollution remediation: Performance, degradation pathway, and toxicity evaluation, J. Environ. Chem. Eng. **13**, 116857 (2025).